Journal of Biomechanics 44 (2011) 2826–2832

Contents lists available at SciVerse ScienceDirect

Journal of Biomechanics

journal homepage: www.elsevier.com/locate/jbiomech
www.JBiomech.com

Direct numerical simulation of transitional flow in a patient-specific intracranial aneurysm

Kristian Valen-Sendstad [a,b,*], Kent-André Mardal [a,b], Mikael Mortensen [c], Bjørn Anders Pettersson Reif [c], Hans Petter Langtangen [a,b]

[a] Center for Biomedical Computing, Simula Research Laboratory, P. O. Box 134, N-1325 Lysaker, Norway
[b] Department of Informatics, University of Oslo, P. O. Box 1080 Blindern, N-0316 Oslo, Norway
[c] Norwegian Defence Research Establishment, P. O. Box 25, N-2027 Kjeller, Norway

ARTICLE INFO

Article history:
Accepted 1 August 2011

Keywords:
Computational fluid dynamics
Blood flow
Direct Numerical Simulation
Turbulence
Middle cerebral artery aneurysm

ABSTRACT

In experiments turbulence has previously been shown to occur in intracranial aneurysms. The effects of turbulence induced oscillatory wall stresses could be of great importance in understanding aneurysm rupture. To investigate the effects of turbulence on blood flow in an intracranial aneurysm, we performed a high resolution computational fluid dynamics (CFD) simulation in a patient specific middle cerebral artery (MCA) aneurysm using a realistic, pulsatile inflow velocity. The flow showed transition to turbulence just after peak systole, before relaminarization occurred during diastole. The turbulent structures greatly affected both the frequency of change of wall shear stress (WSS) direction and WSS magnitude, which reached a maximum value of 41.5 Pa. The recorded frequencies were predominantly in the range of 1–500 Hz. The current study confirms, through properly resolved CFD simulations that turbulence can occur in intracranial aneurysms.

1. Introduction

Stroke is a leading cause of death in the Western world (Feigin, 2005). One reason for stroke is the rupture of aneurysms usually found in or near the Circle of Willis, an arterial network located at the base of the brain. It is estimated that 1–6% of the population will harbor aneurysms during their lifetime (Schievink, 1997), and that the average risk of rupture is 1–2% annually (Rinkel et al., 1998). The initiation, growth, and rupture of intracranial aneurysms is a complex and multi-factorial process. Population studies have shown that aneurysm rupture is influenced by, e.g., age, gender, smoking, alcohol consumption, hormonal factors, and a mother's age when the first child is born, cf. (Eden et al., 2008; Kongable et al., 1996; Mhurchu et al., 2001; Brisman et al., 2006; Weir, 2002; Schievink, 1997; Longstreth et al., 1994; Humphrey, 2001). The precise mechanism however is still not known. It is well-known that arteries remodel themselves according to flow conditions (Chien, 2007). For example, blood vessels thicken if blood pressure rises, is lengthened with axial loads, or increase internal diameter with high values of WSS. In addition, if the WSS exceeds a limit of 40 Pa, the endothelial cells are believed to be damaged, and an aneurysm might form (Davies et al., 1986; Fry, 1968).

Blood flow in cerebral arteries is a complex phenomenon. Establishing adequate computational flow models that are of clinical relevance has been an active area of research the last decades. Many studies focus on the relevance of nonlinear rheology (Johnston et al., 2006; Fisher and Rossmann, 2009; Kim et al., 2008; Gijsen et al., 1999; Lee and Steinman, 2007; Galdi et al., 2008), and perhaps the most active area is interaction between blood flow and elastic vessel walls (Gerbeau et al., 2005; Heil, 2004; Bazilevs et al., 2010). There has been remarkably little focus on the presence of turbulence in cerebral arteries, and the assumption of laminar flow is commonly accepted. The clinical relevance of determining whether a flow is turbulent is revealed when examining the effects of turbulent flows. A turbulent flow may produce highly increased magnitude of WSS, increased frequency at which the WSS changes direction and local pressure fluctuations. The resulting cell remodeling under such flow conditions is currently unknown.

Turbulence has previously been shown to occur both in the aorta (Khanafer et al., 2007) and in a stenosed carotid artery (Lee et al., 2008). Audible sound, which implies turbulence, has successfully been recorded from saccular aneurysms in dogs (Sekhar et al., 1990) and humans (Ferguson, 1970; Kurokawa et al., 1994). The lowest recorded Reynolds number where turbulence occurred, Re_c, in glass models of human intracranial

* Corresponding author at: Center for Biomedical Computing, Simula Research Laboratory, P. O. Box 134, N-1325 Lysaker, Norway
E-mail address: kvs@simula.no (K. Valen-Sendstad).

0021-9290/$ - see front matter © 2011 Elsevier Ltd. All rights reserved.
doi:10.1016/j.jbiomech.2011.08.015

arteries (Roach et al., 1972), was less than 500 with a bifurcation angle of 180° and an aneurysm present in the bifurcation. This result strongly contrasts the commonly accepted Re_c=2300 in stationary pipe flow (White, 1999).

There seems to be a gap between the cited experiments and the most of the hemodynamic simulations that are performed. The current work will therefore address the presence of turbulence in an middle cerebral artery (MCA) aneurysm. The motion of a fluid is mathematically described by the Navier–Stokes equations, and a Direct Numerical Simulation (DNS) is performed if all characteristic scales of a turbulent flow are included in the simulation (Wilcox, 2002; Pope, 2000; Durbin and Reif, 2001). A properly executed DNS can capture physically complex phenomenon like transition to turbulence and relaminarization. The objective of the present study is to determine if turbulence can occur in an intracranial MCA aneurysm, and to determine the effects of the turbulence on the aneurysm wall, using DNS.

2. Methodology

2.1. Imaging and patient data

An MCA aneurysm from a patient treated at the Department of Neurosurgery, University Hospital of North Norway during the period 2006–2008 was chosen for patient-specific modeling. The aneurysm was retrieved by searching for MCA aneurysms in an aneurysm quality register, cf. (Lindekleiv et al., 2009). The register was approved by the local ethics committee and the data inspectorate, and the involved patient gave consent for the use of imaging and clinical data. Three-dimensional (3D) imaging of the intracranial arteries and the aneurysm was obtained by computed tomography angiography (CTA). The CTA examination was performed on a 16 multi-detector row spiral computed tomography scanner (Somatom Sensation 16, Siemens, Erlangen, Germany).

The patient-specific geometry was recreated on a computational mesh using the Vascular Modeling Toolkit (Vascular Modeling Toolkit, 2004). The geometry is shown in Fig. 1. We included as much as possible from the vessel to create realistic inlet and outlet conditions (Castro et al., 2006). In addition, the vessels have been extrapolated with a length of 10 diameters to reduce the boundary artifacts influencing the flow. Three computational mesh sizes consisting of 1, 3.1 and 5.5 million tetrahedrons were used. To assess whether or not the flow field was properly resolved, the grid resolution was quantified in terms of the viscous length scale, computed as

$$l^+ \equiv \frac{u_* \Delta l}{\nu}. \tag{1}$$

Here, Δl is a local length scale that represents the averaged extent of the tetrahedron grid cell $\Delta l = 12/\sqrt{2}\Delta_{\mathrm{Vol}}^{1/3}$, where Δ_{Vol} is the tetrahedron volume. The friction velocity, u_*, is given as

$$u_*^2 = \frac{\mu}{\rho}(S_{ij}S_{ij})^{1/2}, \quad S_{ij} = \frac{1}{2}\left(\frac{\partial u_i}{\partial x_j} + \frac{\partial u_j}{\partial x_i}\right), \quad i,j = 1,2,3, \tag{2}$$

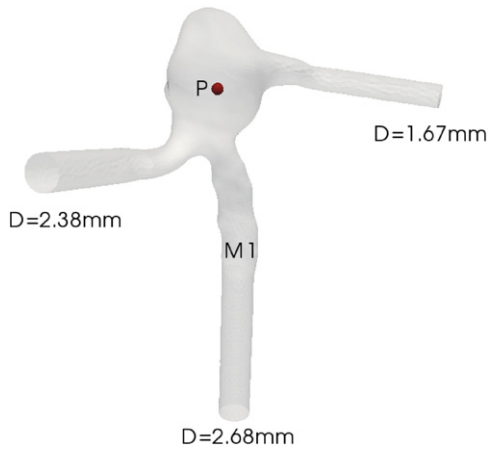

Fig. 1. Patient-specific geometry illustrated as a 20% opaque surface. The sphere, P, indicate where the velocity and pressure have been measured. The parent artery is the M1 segment of the MCA and '*D*' indicates the diameters.

where S_{ij} is the shear deformation rate and where Einstein's summation convention is used. If $l^+ = 1$, then the average grid size Δl equals the viscous length scale which is the smallest spatial scale at which turbulent fluctuations can persist. Since we are not considering an almost unidirectional flow, the usual classifications of the viscous scales in three different spatial dimensions are not straightforward (Durbin and Reif, 2001; Pope, 2000; Wilcox, 2002). Instead we have assumed that $l^+ \sim O(1)$ in any direction is sufficient as an indication of a proper grid resolution. Inside the aneurysm dome $l^+ \sim 2$ on the finest mesh. Similarly, we computed

$$t^+ \equiv \frac{\nu}{u_*^2}, \tag{3}$$

where t^+ is the smallest time scale in a turbulent flow. In our simulation $t^+ \leq 2.2$.

The diameter of the aneurysm is 8.2 mm and the height is 9.1 mm, measured when the dome was extracted from the artery, similar to Ford et al. (2009). The parent artery is the M1 segment of the MCA and has the diameter (D) 2.68 mm. The daughter vessels are 2.38 and 1.67 mm in diameter respectively. Based on the parent artery in Fig. 1 and the inflow velocity (U) in Fig. 2 the corresponding mean and maximum Reynolds numbers (UD/ν) are 436 and 697 respectively, where the kinematic viscosity is $\nu = \mu/\rho$, see Section 2.2. With a heart rate of 60 beats per minute, the angular frequency (ω) is 0.002 π/ms, and the Womersley number, $D/2(\omega/\nu)^{1/2}$, is 1.8.

2.2. Computational fluid dynamics simulations

To simulate the flow, we solved the incompressible Navier–Stokes equations (Durbin and Reif, 2001; White, 1999), using the numerical solver CDP (CDP), which is a finite volume code developed at Stanford University. CDP uses a second order accurate node-based finite volume discretization in space and advances the equations in time using a second order accurate incremental pressure corrections scheme (Goda, 1979), with Adams–Bashforth treatment of the convective term, and a (midpoint) Crank–Nicolson discretization for the diffusive term. The blood density and viscosity were set to $\rho = 1025$ kg/m^3 and $\mu = 0.0035$ Pa s, respectively. The time step was set in reference to the smallest mesh sizes and varied from 0.1, 0.05 to 0.025 ms. Since the smallest viscous scales of the flow can be assumed to be resolved, no explicit turbulence model was applied. The simulations were performed on 32 CPUs, and each cardiac cycle required 12 h of computational time, resulting in roughly 5000 CPU hours. Due to the computational cost, we were restricted to simulating 13 heartbeats, where the reported values are taken from the last 12 cycles computed on the finest grid.

2.3. Boundary conditions

Fig. 2 shows the waveform from a patient of equivalent age, which was used as the inflow boundary condition. The values have been adjusted to fit the minimum, mean and maximum values obtained by Krejza et al. (2005) where the MCA velocities of 335 people were measured. It should be noted that any transition occurring inside the aneurysm is most likely caused by local flow conditions rather than pre-determined fluctuating modes of the inflow boundary conditions, see Fig. 2. On the outlets we used a non-reflecting boundary condition with an equal flux division between the daughter vessels. This particular choice was made since the pressure drop in the main cerebral arteries, such as in the MCA, is

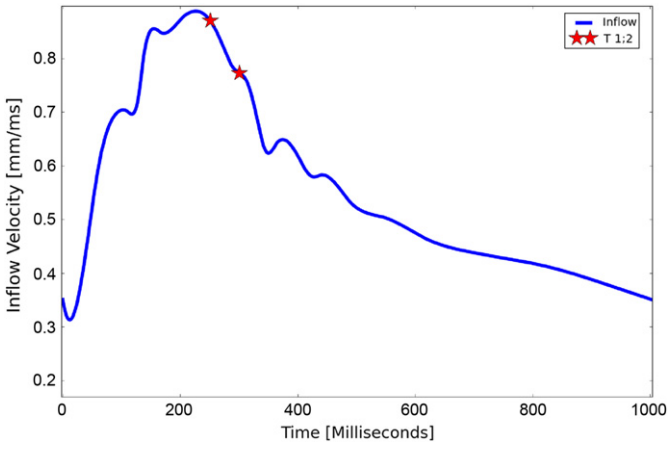

Fig. 2. The figure shows the inflow velocity profile with red points indicating the time from where Figs. 3, 4 and 8 are made at T1=250 ms and T2=300 ms. (For interpretation of the references to color in this figure legend, the reader is referred to the web version of this article.)

dominated by the resistance in the complex downstream vasculature, cf. (Alastruey et al., 2007; Vignon-Clementel et al., 2006).

2.4. Turbulent kinetic energy

To derive the specific turbulent kinetic energy (TKE), we decompose an instantaneous velocity component, u_i, as,

$$u_i = \overline{u}_i + u_i', \tag{4}$$

where $\overline{u}_i$ and u_i' are the mean and fluctuating velocity components respectively in the x_i direction. The TKE is then defined as:

$$k = \tfrac{1}{2}\overline{(u_i' u_i')}, \tag{5}$$

where the overline represents ensemble (phase) average quantities.

2.5. Convergence tests

To assess whether or not the resolutions in both space and time are sufficient, we also measured the integral of the (pseudo) dissipation rate (E) within the computational domain (Pope, 2000, Chapter 5),

$$E = \int_\Omega \varepsilon \, d\Omega, \tag{6}$$

where $\varepsilon = \nu(\overline{(\partial u_i/\partial x_j)(\partial u_i/\partial x_j)})$. For the two finest meshes with the time step set to 0.025 milliseconds, E varied with less than 1% between the meshes. Combined with $l^+ \sim 2$ and $t^+ \leq 2.2$, we considered this to be sufficient evidence that all spatial and temporal scales were adequately resolved.

3. Simulation results

3.1. Flow

The parent artery bends slightly and the flow entered the dome at an angle. Due to a narrowing of the parent artery just before the aneurysm dome, the velocity field exhibited a local maximum just after entering the aneurysm. The flow was similar at the start and end of the heart cycle, with a single vortex in the center of the domain. However, during the heart cycle the position where the flow impinged onto the opposing wall changed and as a consequence the entire flow changed. From peak systole through to the deceleration phase several complex vortical structures arose. The flow underwent several regimes from laminar, to transitional, turbulent, then finally back to laminar again. The flow patterns at the specific times indicated in Fig. 2, are shown in Fig. 3. The vorticity, $\vec{\omega} \equiv \nabla \times \vec{u}$, is shown as a scalar field in Fig. 4, and illustrates highly complex turbulent structures which are dampened towards diastole. In Fig. 5 measurements from two cycles in P of all three velocity components (top), as well as pressure is shown. The peak pressure fluctuations are at roughly 200 Pa which corresponds to 1.5 mmHg, at a frequency of 100 Hz.

3.2. Turbulent kinetic energy

Fig. 5 shows the three velocity components measured in P for two cardiac cycles, cf. Fig. 1. The flow is highly complex, and analysis revealed that the flow exhibits a transition to turbulence after peak systole. This can be explained by the fact that during the acceleration phase local flow instabilities were dampened, whereas during the deceleration phase, the instabilities had a tendency to grow. This is fully consistent with earlier findings (Juárez and Ramos, 2003), and visible in Fig. 6 where the u_1 component of the velocity from the last four cycles has been superimposed. The flow is highly complex, and differed significantly after peak systole. The ensemble averaged TKE measured in P obtained from 12 cycles is shown in Fig. 7 (top), along with the corresponding frequency spectrum (bottom) of the last 3/4 cycle. The results in Fig. 7 confirm that the flow remains laminar until peak systole and that the peak turbulent kinetic energy occurs roughly 100 ms after peak systole. The frequency spectrum shows that the flow exhibits time variations up to about 5000 Hz.

3.3. Wall shear stress

The WSS in this aneurysm had a peak value of 41.5 Pa where the flow impinged at peak systole, but the peak WSS value and the impingement point changed throughout the cycle. At the back of the aneurysm dome, relative to where the flow impinged, the flow was highly oscillatory and the WSS showed complex, chaotic behavior in time and space. By comparing regions of the aneurysm dome at different time steps, it is clear that the WSS direction changes several times during a heartbeat. Fig. 8 shows the WSS magnitude at the surface of the aneurysm. The highly complex and detailed WSS pattern changes significantly during only 50 ms, as can be seen at T1 to the left and T2 to the right in Fig. 8.

4. Discussion

In the aneurysm used in the current study, there are three main reasons why the flow exhibited a non-laminar behavior. First, the volume of the aneurysm dome is relatively large, 264 mm^3. As the blood entered the dome, the increased volume

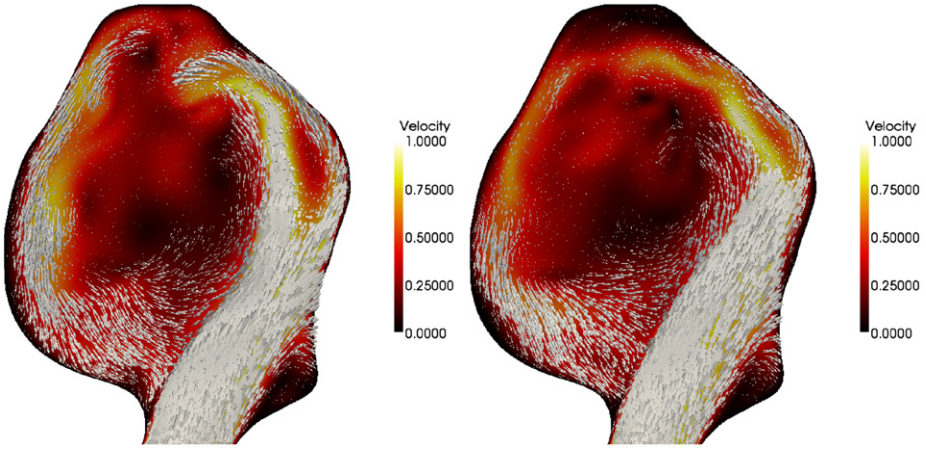

Fig. 3. Flow patterns [mm/ms] visualized as a slice through the aneurysm dome with arrows indicating flow direction at times T1–T2. The direction and magnitude of the velocity vectors change significantly both in the center of the dome and in the high curvature regions near the wall. Recirculation zones also appear and disappear with time, in the latter regions.

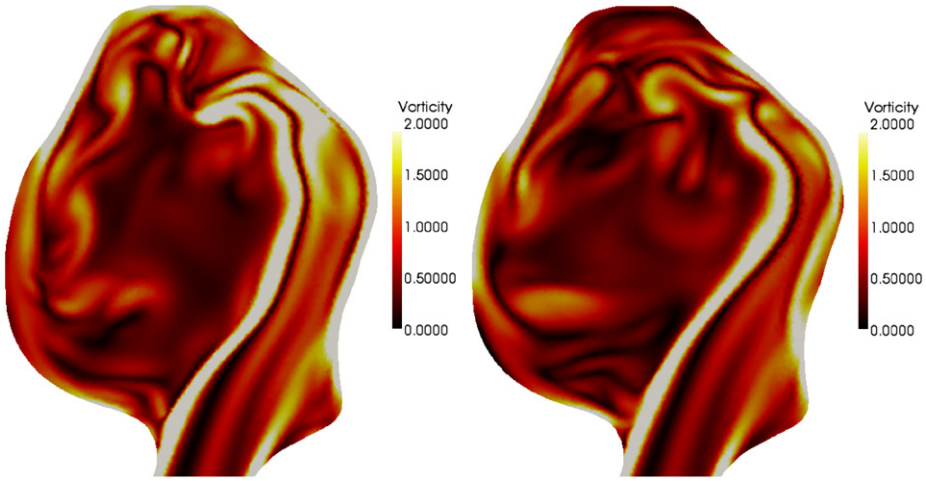

Fig. 4. The magnitude of the vorticity [1/ms] is visualized as a slice through the aneurysm dome at times T1–T2.

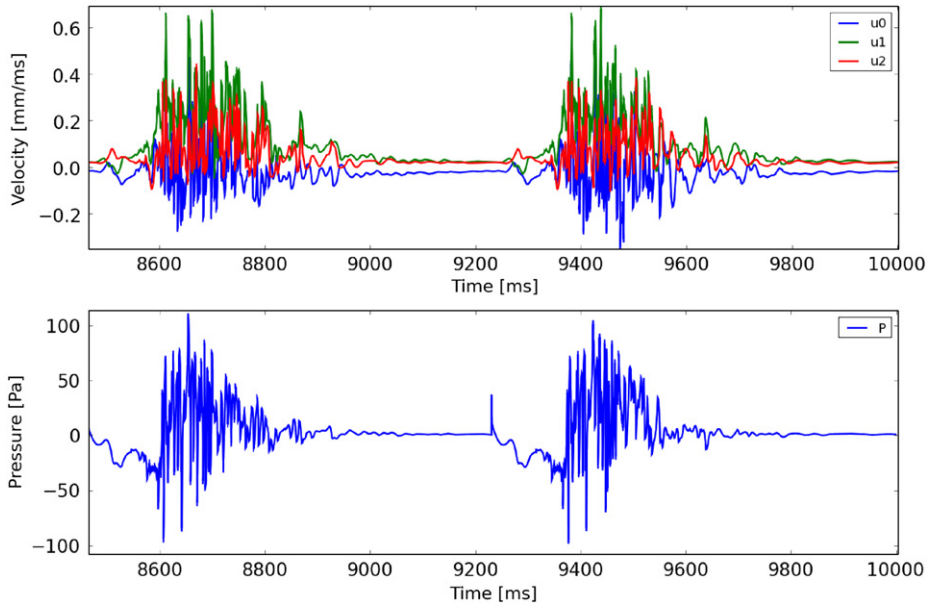

Fig. 5. The top half of the figure shows velocity measurements in u_0,u_1 and u_2 directions for the point P shown in Fig. 1 over two heartbeats. The bottom half of the figure is the corresponding pressures at this location.

resulted in less confinement of the jet and the flow therefore had an increased tendency to become more unstable. Second, strong shear forces developed due to the large velocity gradients, as the high speed flow entered the dome. This caused the flow field to undergo shear induced instabilities. Third, the shear instabilities, which are of the Kelvin–Helmoltz type, resulted in a series of (primary) vortices which dominates the dynamics of the jet. After these impinge on the aneurysm wall they lead to an unsteady separation, cf. (Popiel and Trass, 1991). All three effects contribute to an increased likelihood for transition to turbulence.

In a previous CFD study of 20 MCA aneurysms, the maximum WSS was found to be 14.39 ± 6.21 Pa (Shojima et al., 2004). The maximum WSS in the current case was significantly higher (41.5 Pa). The exact reasons for these differences are not known, but it could be the patient-specific geometry. In Shojima et al. (2004) the average mesh consisted of 60.000 hexahedral elements and a time step of 10^{-4} s, whereas here we use 5.5 million tetrahedrons and a time step of 2.5×10^{-5} s. This time step could not have been larger, since the flow had only just been fully resolved.

The other main difference is the boundary conditions, which have been a focus of research in recent years. In Shojima et al. (2004), a traction-free boundary condition was applied at the outlets, whereas we have applied an equal mass flux on the outlets, more consistent with Alastruey et al. (2007). The computed flow is obviously sensitive to the choice of boundary conditions, and the results will therefore be conditional to the outflow boundary conditions. The outflow in this paper is discussable, but measurements are often not available or difficult to perform. More advanced models have been proposed in, e.g., (Alastruey et al., 2007; Vignon-Clementel et al., 2006; Olufsen et al., 2002; Olufsen, 1999; Alastruey et al., 2008; Steele et al., 2007). Tests revealed however that the main finding in the current study, which is that the flow shows transition to turbulence, does not change.

The present study has been limited to a Newtonian description of the blood, but the effects on the flow are believed to be small for arteries in the vicinity of the Circle of Willis (Lee and Steinman, 2007). We have also assumed rigid, impermeable walls when the actual process involves an interaction between the

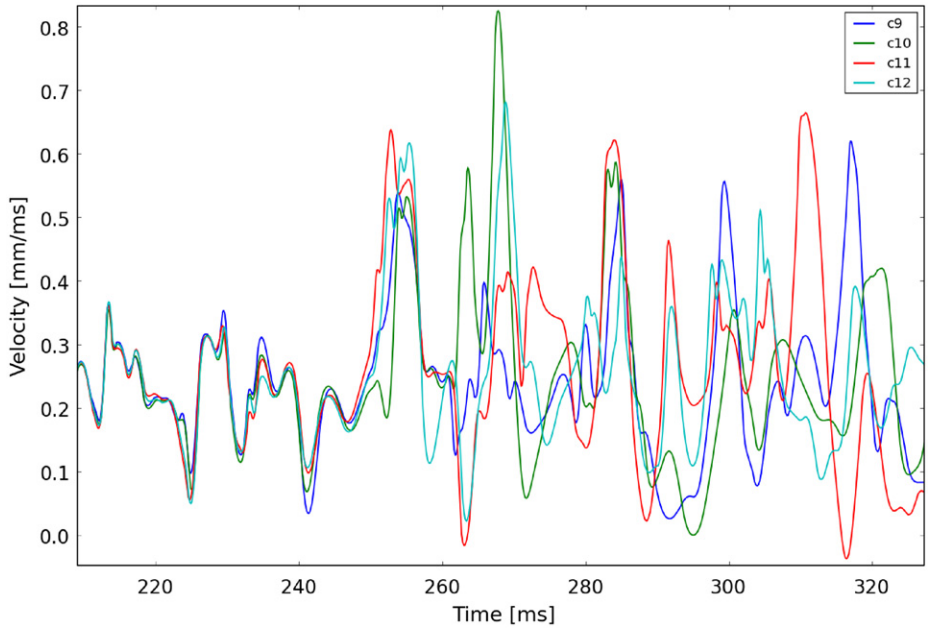

Fig. 6. The figure shows the u_1 velocity component, measured in P, from the last four cycles (labeled c9–c12) for a small period of time close to peak systole which occurs at $t=226$ ms. Small cycle to cycle variations occur just before peak systole (TKE is less than 10^{-4}), but differ greatly as the inflow decelerates, cf. Fig. 7. This departure between the signals quantifies the existence of turbulence.

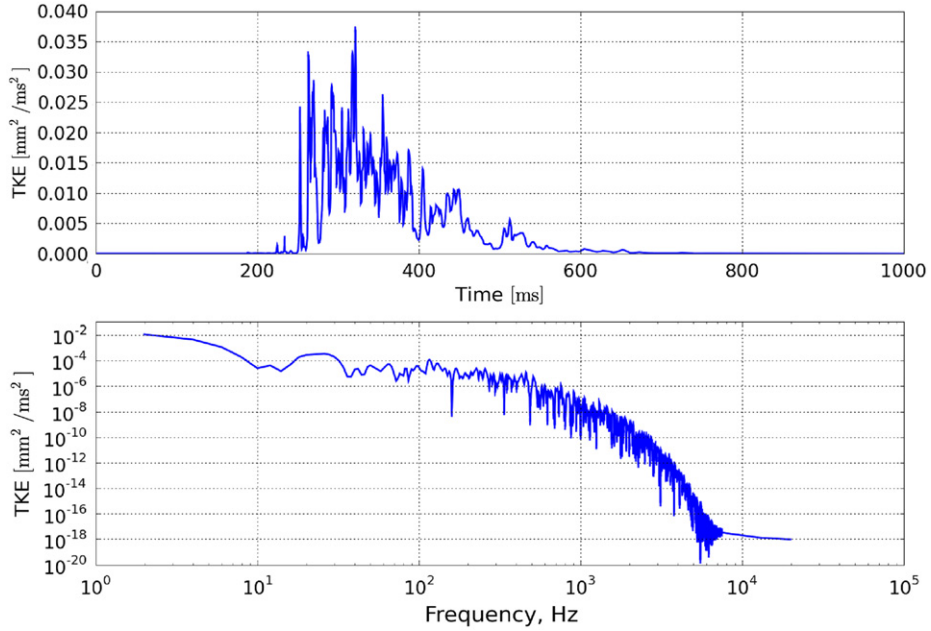

Fig. 7. The top half of the figure shows the average TKE based on 12 cycles, and the bottom half of the figure is the frequency spectrum.

blood flow and the surrounding tissue. The relative wall displacement in MCA aneurysms has previously been shown to be 10–15% (Bazilevs et al., 2010). Additionally, since patient-specific flow rates were not available, we used a realistic waveform with average flow rates taken from Krejza et al. (2005).

Recent DNS simulations of hemodynamics have shown that the turbulent kinetic energy might produce eddies that approach the length scales of red blood cells (RBC) which are 8 μm in diameter. As pointed out by Antiga and Steinman (2009) it is highly likely that viscous effects due to RBC interaction will occur, and a DNS where the smallest length scales approach RBC might therefore produce unreliable results. In the current study, the smallest length scales were $\eta \sim 0.065$ mm which was roughly eight times larger than the RBC diameter.

We have demonstrated computationally that turbulence can be present in an intracranial aneurysm. Consequently, turbulence and its subsequent effects on the arterial wall should be considered in future simulations to describe the blood flow adequately.

Conflict of interest statement

There is no conflict of interest for all authors.

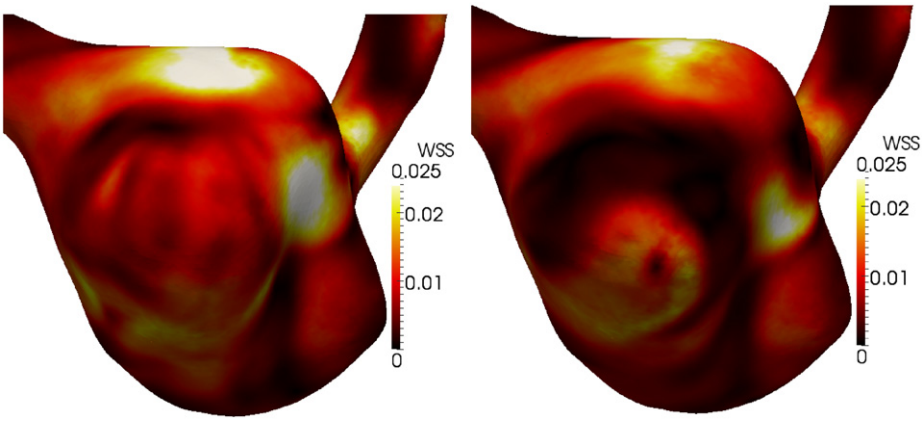

Fig. 8. WSS [g/ms^2 mm] at times T1 (left) and T2 (right) at the top of the aneurysm dome shows how the flow changes significantly over the short time span of 50 ms.

Acknowledgements

We gratefully acknowledge fruitful discussions with Emeritus Professor Charles M. Strother, MD, and Research Fellow Dr. Jinfeng Jiang at Wisconsin Institutes for Medical Research. The work has been supported by a Center of Excellence grant from the Research Council of Norway to Center for Biomedical Computing at Simula Research Laboratory.

References

Alastruey, J., Parker, K., Peiro, J., Byrd, S., Sherwin, S., 2007. Modelling the Circle of Willis to assess the effects of anatomical variations and occlusions on cerebral flows. Journal of Biomechanics 40 (8), 1794–1805.

Alastruey, J., Moore, S.M., Parker, K.H., David, T., Peiro, J., Sherwin, S.J., 2008. Reduced modelling of blood flow in the cerebral circulation: coupling 1-d, 0-d and cerebral auto-regulation models. International Journal for Numerical Methods in Fluids 56 (8), 1061–1067.

Antiga, L., Steinman, D.A., 2009. Rethinking turbulence in blood. Biorheology 46 (2), 77–81.

Bazilevs, Y., Hsu, M.-C., Zhang, Y., Wang, W., Kvamsdal, T., Hentschel, S., Isaksen, J., 2010. Computational vascular fluid–structure interaction: methodology and application to cerebral aneurysms. Biomechanics and Modeling in Mechanobiology 9, 481–498.

Brisman, J.L., Song, J.K., Newell, D.W., 2006. Cerebral aneurysms. The New England Journal of Medicine 355 (9), 928–939.

Castro, M., Putman, C., Cebral, J., 2006. Computational fluid dynamics modeling of intracranial aneurysms: effects of parent artery segmentation on intraaneurysmal hemodynamics. American Journal of Neuroradiology 27 (8), 1703–1709.

CDP, 〈http://www.stanford.edu/group/cits/research/combustor/cdp.html〉.

Chien, S., 2007. Mechanotransduction and endothelial cell homeostasis: the wisdom of the cell. American Journal of Physiology – Heart and Circulatory Physiology 292 (3), H1209–H1224.

Davies, P.F., Remuzzi, A., Gordon, E.J., Dewey, C.F., Gimbrone, M., 1986. Turbulent fluid shear stress induces vascular endothelial cell turnover in vitro. Proceedings of the National Academy of Science USA 83, 2114–2117.

Durbin, P., Reif, B.A.P., 2001. Statistical Theory and Modeling for Turbulent Flows. Wiley & Sons.

Eden, S., Meurer, W., Sanchez, B., Lisabeth, L., Smith, M., Brown, D., Morgenstern, L., 2008. Gender and ethnic differences in subarachnoid hemorrhage. Neurology 71, 731–735.

Feigin, V., 2005. Stroke epidemiology in the developing world. The Lancet 365, 2160–2161.

Ferguson, G.G., 1970. Turbulence in human intracranial saccular aneurysms. Journal of Neurosurgery 33 (5), 485–497.

Fisher, C., Rossmann, J.S., 2009. Effect of non-Newtonian behavior on hemodynamics of cerebral aneurysms. Journal of Biomechanical Engineering 131 (9), 091004.

Ford, M.D., Hoi, Y., Piccinelli, M., Antiga, L., Steinman, D.A., 2009. An objective approach to digital removal of saccular aneurysms: technique and applications. British Journal of Radiology 82, S55–S61 (Special Issue 1).

Fry, D.L., 1968. Acute vascular endothelial changes associated with increased blood velocity gradients. Circulation Research 22 (2), 165–197.

Galdi, G.P., Robertson, A.M., Rannacher, R., Turek, S., Robertson, A.M., Sequeira, A., Kameneva, M.V., 2008. Hemorheology. Hemodynamical Flows. Oberwolfach Seminars, vol. 37. Birkhuser, Basel, pp. 63–120.

Gerbeau, J., Vidrascu, M., Frey, P., 2005. Fluid–structure interaction in blood flows on geometries based on medical imaging. Computers & Structures 83 (2–3), 155–165.

Gijsen, F.J.H., van de Vosse, F.N., Janssen, J.D., 1999. The influence of the non-newtonian properties of blood on the flow in large arteries: steady flow in a carotid bifurcation model. Journal of Biomechanics 32 (6), 601–608.

Goda, K., 1979. A multistep technique with implicit difference schemes for calculating two- or three-dimensional cavity flows. Journal of Computational Physics 30 (1), 76–95.

Heil, M., 2004. An efficient solver for the fully coupled solution of large-displacement fluid-structure interaction problems. Computer Methods in Applied Mechanics and Engineering 193 (1–2), 1–23.

Humphrey, J.D., 2001. Cardiovascular Solid Mechanics. Springer.

Johnston, B.M., Johnston, P.R., Corney, S., Kilpatrick, D., 2006. Non-Newtonian blood flow in human right coronary arteries: transient simulations. Journal of Biomechanics 39 (6), 1116–1128.

Juárez, L.H., Ramos, E., 2003. Direct numerical simulation of transition to turbulence in an oscillatory channel flow. Comptes Rendus Mecanique 331 (1), 55–60.

Khanafer, K.M., Bull, J.L., Upchurch, G.R., Berguer, R., 2007. Turbulence significantly increases pressure and fluid shear stress in an aortic aneurysm model under resting and exercise flow conditions. Annals of Vascular Surgery 21 (1), 67–74.

Kim, Y.H., VandeVord, P.J., Lee, J.S., 2008. Multiphase non-Newtonian effects on pulsatile hemodynamics in a coronary artery. International Journal for Numerical Methods in Fluids 58 (10), 803–825.

Kongable, G., Lanzino, G., Germanson, T., Truskowski, L., Alves, W., Torner, J., Kassell, N., 1996. Gender-related differences in aneurysmal subarachnoid hemorrhage. Journal of Neurosurgery 84, 43–48.

Krejza, J., Szydlik, P., Liebeskind, D.S., Kochanowicz, J., Bronov, O., Mariak, Z., Melhem, E.R., 2005. Age and sex variability and normal reference values for the VMCA/VICA index. AJNR American Journal of Neuroradiology 26 (4), 730–735.

Kurokawa, Y., Abiko, S., Watanabe, K., 1994. Noninvasive detection of intracranial vascular lesions by recording blood flow sounds. Stroke 25 (2), 397–402.

Lee, S.E., Lee, S.-W., Fischer, P.F., Bassiouny, H.S., Loth, F., 2008. Direct numerical simulation of transitional flow in a stenosed carotid bifurcation. Journal of Biomechanics 41 (11), 2551–2561.

Lee, S.W., Steinman, D.A., 2007. On the relative importance of rheology for image-based CFD models of the carotid bifurcation. Journal of Biomechanical Engineering 129, 273–278.

Lindekleiv, H.M., Jacobsen, E.A., Kloster, R., Sandell, T., Isaksen, J.G., Romner, B., Ingebrigtsen, T., Bajic, R., 2009. Introduction of endovascular embolization for intracranial aneurysms in a low-volume institution. Acta Radiologica 50 (7), 555–561.

Longstreth, W., Nelson, L., Koepsell, T., vanBelle, G., 1994. Subarachnoid hemorrhage and hormonal factors in women. A population-based case-control study. Annals of Internal Medicine 121, 168–173.

Mhurchu, C., Anderson, C., Jamrozik, K., Hankey, G., Dunbabin, D., 2001. Hormonal factors and risk of aneurysmal subarachnoid hemorrhage: an international population-based, case-control study. Stroke 32, 606–612.

Olufsen, M.S., 1999. Structured tree outflow condition for blood flow in larger systemic arteries. American Journal of Physiology – Heart and Circulatory Physiology 276 (1), H257–H268.

Olufsen, M.S., Nadim, A., Lipsitz, L.A., 2002. Dynamics of cerebral blood flow regulation explained using a lumped parameter model. American Journal of Physiology – Regulatory, Integrative and Comparative Physiology 282 (2), R611–R622.

Pope, S.B., 2000. Turbulent Flows. Cambridge University Press.

Popiel, C.O., Trass, O., 1991. Visualization of a free and impinging round jet. Experimental Thermal and Fluid Science 4 (3), 253–264.

Rinkel, G.J.E., Djibuti, M., Algra, A., van Gijn, J., 1998. Prevalence and risk of rupture of intracranial aneurysms: a systematic review. Stroke 29 (1), 251–256.

Roach, M.R., Scott, S., Ferguson, G.G., 1972. The hemodynamic importance of the geometry of bifurcations in the circle of willis (Glass Model Studies). Stroke 3 (3), 255–267.
Schievink, W.I., 1997. Intracranial aneurysms. The New England Journal of Medicine 336 (1), 28–40.
Sekhar, L., Sun, M., Bonaddio, D., Sclabassi, R., 1990. Acoustic recordings from experimental saccular aneurysms in dogs. Stroke 21 (8), 1215–1221.
Steele, B.N., Olufsen, M.S., Taylor, C.A., 2007. Fractal network model for simulating abdominal and lower extremity blood flow during resting and exercise conditions. Computer Methods in Biomechanics and Biomedical Engineering 10 (1), 39–51.
Shojima, M., Oshima, M., Takagi, K., Torii, R., Hayakawa, M., Katada, K., Morita, A., Kirino, T., 2004. Magnitude and role of wall shear stress on cerebral aneurysm: computational fluid dynamic study of 20 middle cerebral artery aneurysms. Stroke 35 (11), 2500–2505.
Vascular Modeling Toolkit, 〈http://vmtk.org/〉.
Vignon-Clementel, I.E., Figueroa, C.A., Jansen, K.E., Taylor, C.A., 2006. Outflow boundary conditions for three-dimensional finite element modeling of blood flow and pressure in arteries. Computer Methods in Applied Mechanics and Engineering 195 (29–32), 3776–3796 (Absorbing Boundary Conditions).
Weir, B., 2002. Unruptured intracranial aneurysms: a review. Journal of Neurosurgery 96 (1), 3–42.
White, F.M., 1999. Fluid Mechanics, 4th ed. McGraw-Hill, International Editions.
Wilcox, D.C., 2002. Turbulence Modeling for CFD. D C W Industries.